APPLIED SCIENCES AND ENGINEERING

Exceptional capacitive deionization rate and capacity by block copolymer–based porous carbon fibers

Tianyu Liu[1], Joel Serrano[1], John Elliott[1], Xiaozhou Yang[1], William Cathcart[1], Zixuan Wang[2], Zhen He[2], Guoliang Liu[1,3]*

Capacitive deionization (CDI) is energetically favorable for desalinating low-salinity water. The bottlenecks of current carbon-based CDI materials are their limited desalination capacities and time-consuming cycles, caused by insufficient ion-accessible surfaces and retarded electron/ion transport. Here, we demonstrate porous carbon fibers (PCFs) derived from microphase-separated poly(methyl methacrylate)-*block*-polyacrylonitrile (PMMA-*b*-PAN) as an effective CDI material. PCF has abundant and uniform mesopores that are interconnected with micropores. This hierarchical porous structure renders PCF a large ion-accessible surface area and a high desalination capacity. In addition, the continuous carbon fibers and interconnected porous network enable fast electron/ion transport, and hence a high desalination rate. PCF shows desalination capacity of 30 mg_{NaCl} g^{-1}_{PCF} and maximal time-average desalination rate of 38.0 mg_{NaCl} g^{-1}_{PCF} min^{-1}, which are about 3 and 40 times, respectively, those of typical porous carbons. Our work underlines the promise of block copolymer–based PCF for mutually high-capacity and high-rate CDI.

INTRODUCTION

The increasing withdrawal and uneven distribution of freshwater have emerged as critical challenges to technological, social, and economic developments (*1*). On account of the vast amount of seawater and the progressive brine ingress in freshwater reservoirs, desalination is a promising approach to addressing the freshwater shortage. Widely practiced techniques such as reverse osmosis and thermal distillation are suitable for processing seawater or brackish water of high salt concentrations but are energy intensive and costly for treating water of low salt concentrations (e.g., <1000 mg liter^{-1}) (*2*, *3*). Alternatively, capacitive deionization (CDI), which removes ions via electrosorption (*4*, *5*) or pseudocapacitive reactions (*6*, *7*), is the most suitable for desalinating water of low salt concentrations.

Porous carbons are primary CDI electrode materials because of their high electrical conductivity, large surface area, tailorable structure, and excellent stability (*8*). Typical examples include activated carbon (AC) (*9*, *10*), graphene aerogels (*11*–*13*), and biomass-derived macroporous carbons (*14*, *15*). Their desalination capacities and rates, however, are yet to be improved. Typical porous carbons exhibit desalination capacity less than 10 mg of NaCl per gram of electrode, and the desalination rate is slower than 1 mg of NaCl per gram of electrode per minute (*8*). The limited desalination capacity and rate are mainly due to their undesirable porous structures. Macroporous carbons have large pores that allow for fast adsorption of ions, but their surface areas are typically of ~100 m^2 g^{-1}, resulting in low desalination capacities (~5 mg$_{NaCl}$ g^{-1}) (*12*). Microporous carbons (e.g., AC) have high surface areas of >1000 m^2 g^{-1}, but their micropore-dominant structures restrict solution infiltration, which subsequently impedes ion diffusion and reduces desalination rate. The sluggish ion transport retards ion electrosorption and prolongs desalination cycles to hours, or even days (*16*). Moreover, the discrete micro-

porous carbon particles or powders (e.g., AC) induce high particle-particle electrical contact resistance, which obstructs electron conduction and further reduces the desalination rate. Last but not least, the retarded ion diffusion decreases the accessibility of ions to small pores (*17*), reduces the effective surface area for ion electro-sorption, and thus lowers the desalination capacity. Considering the limited performances of macroporous and microporous materials, we hypothesize that carbon fibers (CFs) with interconnected hierarchical mesopores and micropores with short diffusion distances could simultaneously achieve both high desalination capacity and high desalination rate. With pore sizes residing between macropores and micropores, mesopores contribute more surface areas than macropores. In addition, the reduced ion-diffusion distances enhance ion accessibility to micropores (*18*–*20*). The mesopores also function as ion diffusion pathways that accelerate ion electrosorption and water infiltration.

Here, we demonstrate porous CFs (PCFs) with abundant, uniform, and continuous mesopores interconnected with micropores as superior electrode materials for CDI. Our innovation is rooted in the design of the carbon electrode precursor at the molecular level. Specifically, we used a block copolymer poly(methyl methacrylate)-*block*-polyacrylonitrile (PMMA-*b*-PAN) to create PCF via electro-spinning, oxidation, stabilization, and pyrolysis. The microphase separation of PMMA-*b*-PAN resulted in a disordered, bicontinuous network composed of PAN and PMMA domains (*21*). The subsequent carbonization of PAN and decomposition of PMMA yielded continuous CFs with uniform and interconnected mesopores (Fig. 1A). The large effective desalination surface area endowed by the abundant and uniform mesopores, as well as the interconnected micropores and N-dopants inherited from PAN enhanced the desalination capacity. Disparate from most porous carbon particulates (*22*) and monoliths (*23*, *24*), the continuous fibrous carbon scaffold and the interconnected mesopore channels ensured rapid electron transport and fast ion diffusion, respectively, which were essential for high-rate desalination. In batch desalination cells without any ion-exchange resins to aid ion electrosorption or to add parasitic masses (e.g., conductive additives), our PCFs achieved a high desalination capacity

[1]Department of Chemistry, Virginia Tech, Blacksburg, VA 24061, USA. [2]Department of Civil and Environmental Engineering, Virginia Tech, Blacksburg, VA 24061, USA. [3]Macromolecules Innovation Institute, and Division of Nanoscience, Virginia Tech, Blacksburg, VA 24061, USA.
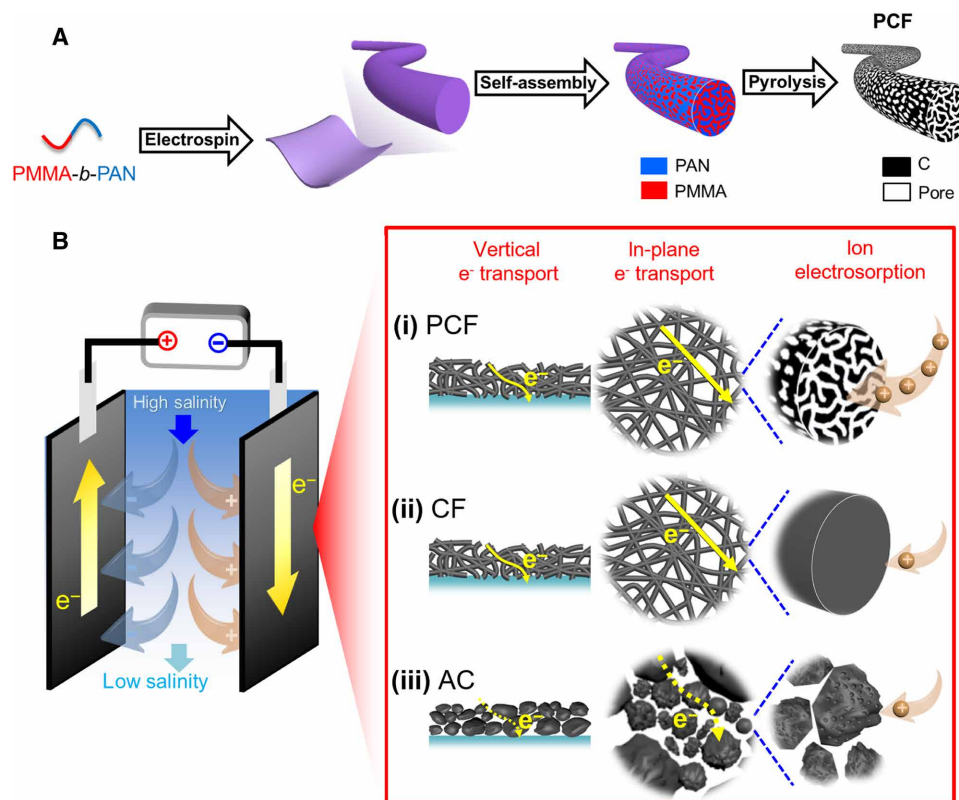*Corresponding author. Email: gliu1@vt.edu

Fig. 1. Schematic illustrations of PCF preparation and capacitive deionization. (**A**) Synthesis of PCF from PMMA-*b*-PAN via electrospinning of PMMA-*b*-PAN into fibers, self-assembly of PMMA-*b*-PAN into disordered, bicontinuous PMMA and PAN domains, and pyrolysis of PMMA-*b*-PAN into PCF with uniform and interconnected pores in a continuous carbon matrix. PMMA generates mesopores and PAN yields carbon. Micropores are also generated in the carbon matrix during the pyrolysis of PAN and are interconnected with the mesopores. (**B**) Scheme of a CDI cell during charging. The CDI electrodes include (i) block copolymer–based PCF, (ii) conventional nonmesoporous CFs, and (iii) AC. (i versus ii) Compared to PAN-derived conventional CFs that are devoid of uniform mesopores, PCF has abundant interconnected mesopores that provide large ion-accessible surface areas and fast ion diffusion. Thus, PCF has a high desalination capacity and high desalination rate. (i versus iii) Compared to AC composed of discrete carbon particles with irregular shapes and sizes, PCF offers continuous electron and ion conduction pathways both in the vertical and in-plane directions that facilitate high-rate deionization.

of 30.4 mg_{NaCl} g_{PCF}^{-1} and an ultrafast desalination rate of 38.0 mg_{NaCl} g_{PCF}^{-1} min^{-1}, surpassing the benchmark AC, conventional CFs from PAN, and other state-of-the-art carbon electrodes under similar experimental conditions.

RESULTS
Materials design principles
To design carbon materials for CDI, we studied three carbon materials (Fig. 1B) including block copolymer–based PCF, industrial standard PAN-based CF, and AC. PCF had uniform and interconnected mesopores originated from the block copolymer microphase separation and PMMA degradation (*21*, *25*, *26*). The uniform mesopores provided PCF with a large ion-accessible surface area. The fibrous carbon and interconnected mesopores served as continuous and effective transport expressways for electrons and ions, respectively, which reduced the internal resistance of desalination cells and improved the desalination rate [Fig. 1B(i)]. In contrast, the mesopore-free CF had a limited surface area for electrosorption of ions [Fig. 1B(ii)]. AC particles had abundant micropores, but the interparticle contact resistance drastically impeded electron transport along both in-plane and vertical directions, resulting in a deteriorated desalination rate [Fig. 1B(iii)]. Moreover, the tortuous microporous network of AC

drastically decreased ion accessibility, which diminished the effective surface area for desalination.

Porous structure and effective desalination surface area
PCF, CF, and AC were adhered to tin-plated copper tapes (3.8 cm by 2.5 cm, Fig. 2, A to C) and used as electrodes in CDI cells. Scanning electron microscopy (SEM) showed distinct morphologies. PCF (Fig. 2D) and CF (Fig. 2E) consisted of intertwined and continuous nanofibers, while AC was made of carbon particles of micrometer sizes and irregular shapes (Fig. 2F). Because of the microphase separation of PMMA-*b*-PAN and the decomposition of PMMA (*21*, *25*, *26*), PCF was perforated with uniform and interconnected mesopores on the surfaces and in the cross section (Fig. 2G), while CF displayed no apparent mesopores (Fig. 2H). The slightly wrinkled skins of CF were caused by rapid solvent evaporation during electrospinning. Under SEM, both the surface and cross section of AC revealed a small number of randomly distributed and irregularly shaped mesopores (Fig. 2I).

N_2 and CO_2 physisorption elucidated the structural details of PCF, CF, and AC. PCF exhibited type IV N_2-sorption isotherm with a hysteresis loop in the relative pressure range of 0.7 to 0.9 (Fig. 3A, red curve), which is a signature of micropores and mesopores (*27*). In contrast, the N_2-physisorption isotherm of CF exhibited
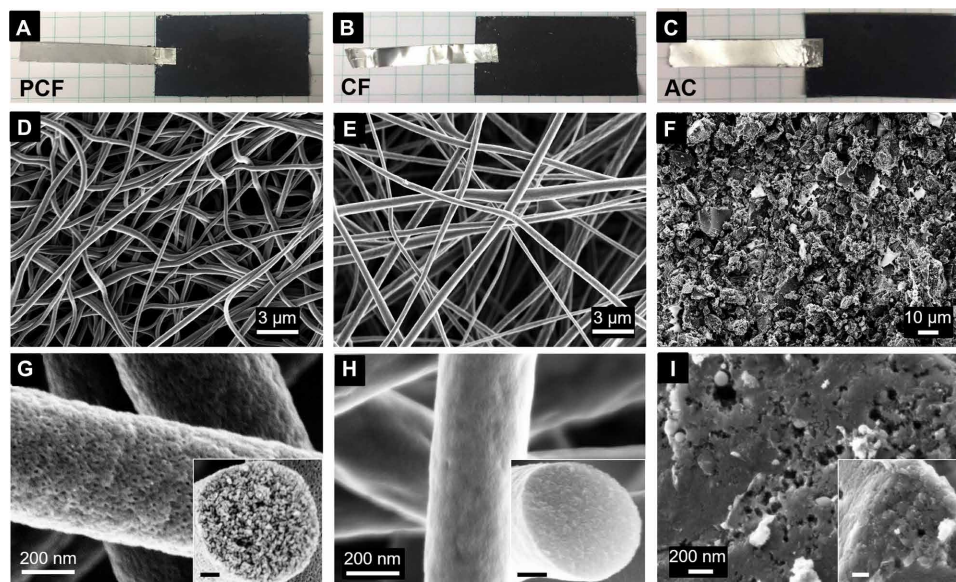
Fig. 2. Structures and morphologies. (**A** to **C**) Photographs of (A) PCF, (B) CF, and (C) AC adhered to Sn tapes. The area of each electrode is ~3.8 cm by 2.5 cm. Photo Credits: Tianyu Liu, Virginia Tech. (**D** to **F**) Low-magnification top-view SEM images of (D) PCF, (E) CF, and (F) AC. PCF and CF are continuous fibers while AC is made of discrete particles. (**G** to **I**) Magnified views of (G) PCF, (H) CF, and (I) AC. (Insets) Cross-sectional images. Scale bars, 100 nm.

no distinct features. The consistently lower adsorption capacity of CF than those of PCF and AC at all relative pressures (Fig. 3A, blue curve) indicated a limited number of pores in CF. The rapid increase in the amount of N_2 adsorbed on AC at relative pressures below 0.2 and the absence of a hysteresis loop in the intermediate relative pressure range in the isotherm (Fig. 3A, black curve) suggested that the pores in AC were predominantly micropores. All three carbon materials displayed type I CO_2-sorption isotherms (Fig. 3B). Notably, the desorption curves of PCF and CF did not fully overlap the corresponding adsorption curves. This irreversible adsorption-desorption behavior was due to the presence of nitrogen heteroatoms (28), as confirmed by x-ray photoelectrical spectroscopy (XPS) (vide infra).

PCF, CF, and AC had different N_2-based Brunauer-Emmett-Teller (BET) surface areas of 639.9, 144.6, and 1317.0 $m^2 g^{-1}$, respectively. Since the surface areas derived from N_2-physisorption at 77 K were unrepresentative of the effective surface area for desalination at room temperature (29), we used CO_2-sorption isotherms to determine their surface areas (Fig. 3C), because they were collected at 273 K that was much closer to the ambient conditions for desalination. The CO_2-based BET surface area of PCF was 132.9 $m^2 g^{-1}$, exceeding those of CF (57.9 $m^2 g^{-1}$) and AC (93.8 $m^2 g^{-1}$). The highest surface area of PCF among the materials studied in this work bestowed its highest capacity for electrosorbing ions into electrical double layers (see fig. S1 and its associated discussions). We further calculated their effective desalination surface areas based on the size of hydrated Na^+ (see Supplementary Methods), which displayed a similar trend to the CO_2-based BET surface areas. The effective desalination surface area of PCF was 127.4 $m^2 g^{-1}$, accounting for 95.9% of the CO_2-based BET surface areas. In contrast, the effective desalination surface areas of CF and AC were 31.8 and 44.1 $m^2 g^{-1}$, corresponding to only 55.0 and 47.0% of the CO_2-based BET surface areas, respectively. The low utilization of the surface areas of CF and AC for desalination was due to the limited ion accessibility to the disorderly arranged micropores (4) (Fig. 3D).

The pore size distributions (PSDs) were extracted by using non-localized density functional theory (NLDFT). PCF had a multi-modal PSD, containing both micropores of 0.5 to 1.2 nm and uniform mesopores of ~12.7 nm (Fig. 3D). The narrowly distributed uniform mesopores resulted from the well-controlled block copolymer microphase separation. In contrast, CF had barely any mesopores but mostly micropores. AC had mesopores, but the pore size was much less uniform than that of PCF. The mesopore size of AC spanned across the entire mesopore range of 2 to 50 nm, as defined by the International Union of Pure and Applied Chemistry (30). A major portion of the mesopores in AC was less than 3.5 nm and peaked at 2.0 nm. Previous reports (17, 31, 32) have shown that micropores impede in-pore ion transport, leading to slow desalination rates that are undesirable for high-rate CDI. On the contrary, mesopores facilitate ion transport owing to their large pore openings (31, 33). Therefore, we expect PCF to exhibit the highest desalination rate.

Chemical and electrical properties

XPS showed that PCF and CF were dual-doped with oxygen and nitrogen, whereas AC only contained oxygen heteroatoms (Fig. 4A and fig. S2, A and B). The O and N heteroatoms in PCF and CF were originated from the oxidative cross-linking and the nitrile group in PAN, respectively (34), and the O atoms in AC could be from either the precursor or the activation processes. Deconvolution of N 1s peaks disclosed that the N atoms were pyridinic-N, graphitic-N, and pyrrolic-N (Fig. 4B and fig. S2C). The functional N heteroatoms were beneficial for CDI: First, the stronger electronegativity of N than C induced charge redistribution around the N atoms, making the electron density of N higher than that of neighboring C atoms (35, 36). The redistributed charges attracted cations/anions and increased the desalination capacity (24). Second, the graphitic-N increased the number of electrons in the conduction band of graphitic regions, which improved electrical conductivity (37). Last, the N
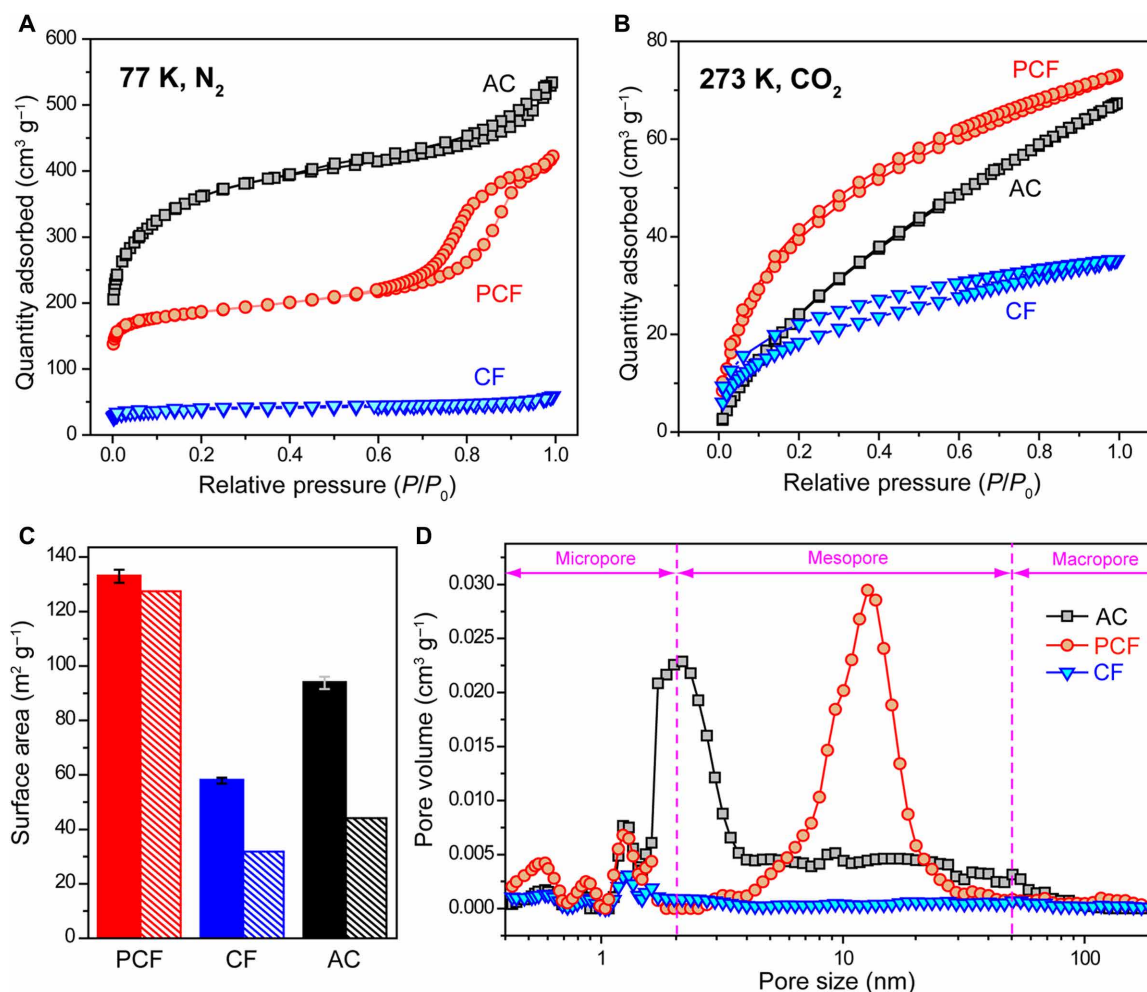
Fig. 3. Characteristics of porous structures. (**A**) N_2 (at 77 K) and (**B**) CO_2 (at 273 K) physisorption isotherms of PCF, CF, and AC. (**C**) Surface areas of PCF, CF, and AC. Solid bars represent the BET surface areas determined from the CO_2 adsorption isotherms, and dashed bars denote the effective desalination surface areas evaluated from the desalination capacity and the radius of hydrated Na^+ (see Supplementary Methods). The error bars are instrument errors. (**D**) PSDs of PCF, CF, and AC determined by nonlinear density functional theory. The dashed vertical line marks the boundary between different pores (i.e., micropores, mesopores, and macropores). The PSDs of the micropores and mesopores are derived from CO_2- and N_2-physisorption isotherms, respectively.

heteroatoms ensured PCF and CF to be highly hydrophilic (Fig. 4C), similar to a previous report (*38*). In contrast, the large water contact angle of ~95° evidenced that AC was hydrophobic, an undesirable property for desalting aqueous solutions.

On the basis of four-point probe measurements and electro-chemical impedance spectroscopy (EIS), PCF and CF without any conductive additives were highly electrically conductive (Fig. 4D). The electrical conductivities of PCF and CF were ~1.0 S cm^{-1} due to the continuous and conductive CFs. In contrast, because the interparticle voids drastically impeded the electron conduction, the conductivity of AC was 10 times lower than those of PCF and CF. In the EIS spectra of the desalination cells (fig. S3, A to D), the combined series resistances (R_s, the Z'-axis intercepts) were consistent with the electrical conductivities. Specifically, the R_s values of PCF and CF cells were 34.9 and 34.6 ohms, respectively, while that of the AC cell was 284.1 ohms. Because all the electrodes were of the same geometrical areas, assembled following the same protocol, and immersed in identical electrolytes [NaCl aqueous solutions (500 mg liter^{-1})],

the different equivalent series resistances (ESRs) were attributed to the different electrical resistances of the carbon materials. The ESR of AC cells was about 10 times higher than those of PCF and CF cells, matching the differences in electrical conductivities. These ESR values were larger than the typical values of carbon electrodes in supercapacitors with concentrated alkaline electrolytes (<5 ohms), mainly due to the much lower electrolyte concentration in desalination cells (in the order of millimolar) than that in supercapacitors (in the order of molar). The high electrical resistance of AC was also reflected by its oval-shaped CV at 100 mV s^{-1} (fig. S3E). CVs of PCF, CF, and AC exhibited no appreciable redox peaks, suggesting that the electrodes desalinated water mainly via electrical double layers.

EIS additionally revealed the diffusion resistances of ions in PCF, CF, and AC. By fitting the intermediate-low frequency range of the Nyquist plots (Supplementary Methods and fig. S3, B to D, for details), we observed that PCF exhibited the smallest diffusion resistance of 223.3 ohm s$^{-0.5}$, whereas those of CF and AC were 1111.7 and 294.2 ohms s$^{-0.5}$, respectively (Fig. 4E). Consequently, PCF had
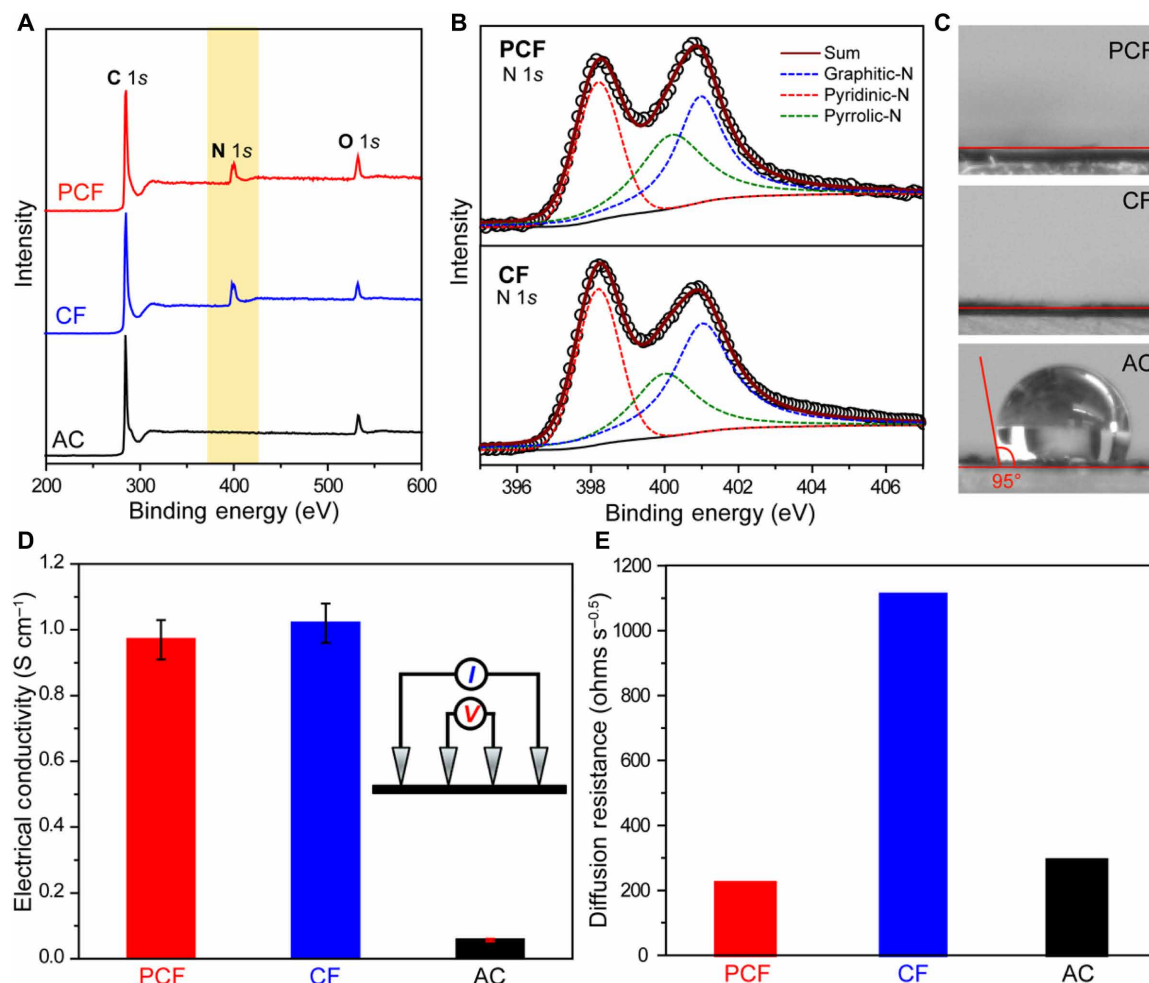
Fig. 4. Chemical and electrical properties. (**A**) XPS survey spectra of PCF, CF, and AC. The light-yellow region highlights the N 1*s* peak. (**B**) The N 1*s* spectra of PCF and CF. The black circles are experimental data. The red, green, and blue dashed peaks represent pyridinic-N, pyrrolic-N, and graphitic-N, respectively. The solid burgundy curves are the best fittings. (**C**) Static contact angles of NaCl solution (500 mg liter^{-1}) on the surfaces of PCF, CF, and AC. (**D**) Electrical conductivities of PCF, CF, and AC measured by a four-point probe. Inset: Scheme of a four-point probe setup. The error bars are standard deviations (SDs) based on at least five independent measurements. Because of the interparticle contact resistance, the electrical conductivity of AC is appreciably lower than those of PCF and CF. (**E**) Na$^+$ diffusion resistances of PCF, CF, and AC probed by electrochemical impedance spectroscopy (EIS) in NaCl solutions (500 mg liter^{-1}).

the best conditions for ion diffusion among the three electrodes (Supplementary Methods and fig. S3F). The drastically different ion diffusion resistances were correlated to the structures of the carbon materials. The micropore-dominating AC and the mesopore-devoid CF impeded ion diffusion within the electrodes. In contrast, the mesopore-dominating and interconnected porous network of PCF allowed for fast ion diffusion, which was indispensable for high-rate desalination. Combining the hierarchical porous structure, high effective surface area, high electrical conductivity, and low ion-diffusion resistance, we anticipate PCF to be an excellent electrode material for CDI.

CDI performances
We first demonstrated the deionization capability of PCF by desalinating two types of waters: artificial brackish water containing NaCl (~1000 mg liter^{-1}) and synthetic tap water containing NaCl (~500 mg liter^{-1}; Fig. 5A and table S1) in conical cells with two symmetric electrodes (fig. S4A). The concentrations were determined

by ion chromatography (fig. S4, B and C). After 10 deionization cycles (+1.0 V, 600 s for each time) using ~15 mg of PCF, 5 ml of brackish water was converted to freshwater with a NaCl concentration of 219.3 ± 4.7 mg liter^{-1}. Similarly, after five deionization cycles, the NaCl concentration of the tap water dropped to an ultralow concentration of 5.5 ± 1.2 mg liter^{-1}.

To further quantify the desalination capacity and rate of PCF, we performed single-cycle deionization with PCF, in comparison with CF and AC, in conical cells with an excess amount (20 ml) of the tap water. With identical carbon mass loadings (~7 mg on each electrode), two symmetric electrodes were submerged in aqueous solutions of NaCl (fig. S4A). An electrical conductivity meter was inserted in the cells to monitor electrical conductivity, which was converted to salt concentration according to calibration curves (fig. S5). To focus on the intrinsic performances of carbon materials rather than engineering of the devices, we selected an initial NaCl concentration of ~500 mg liter^{-1}, because the modified Donnan model predicted that porous carbons perform the best at this concentration. This optimal
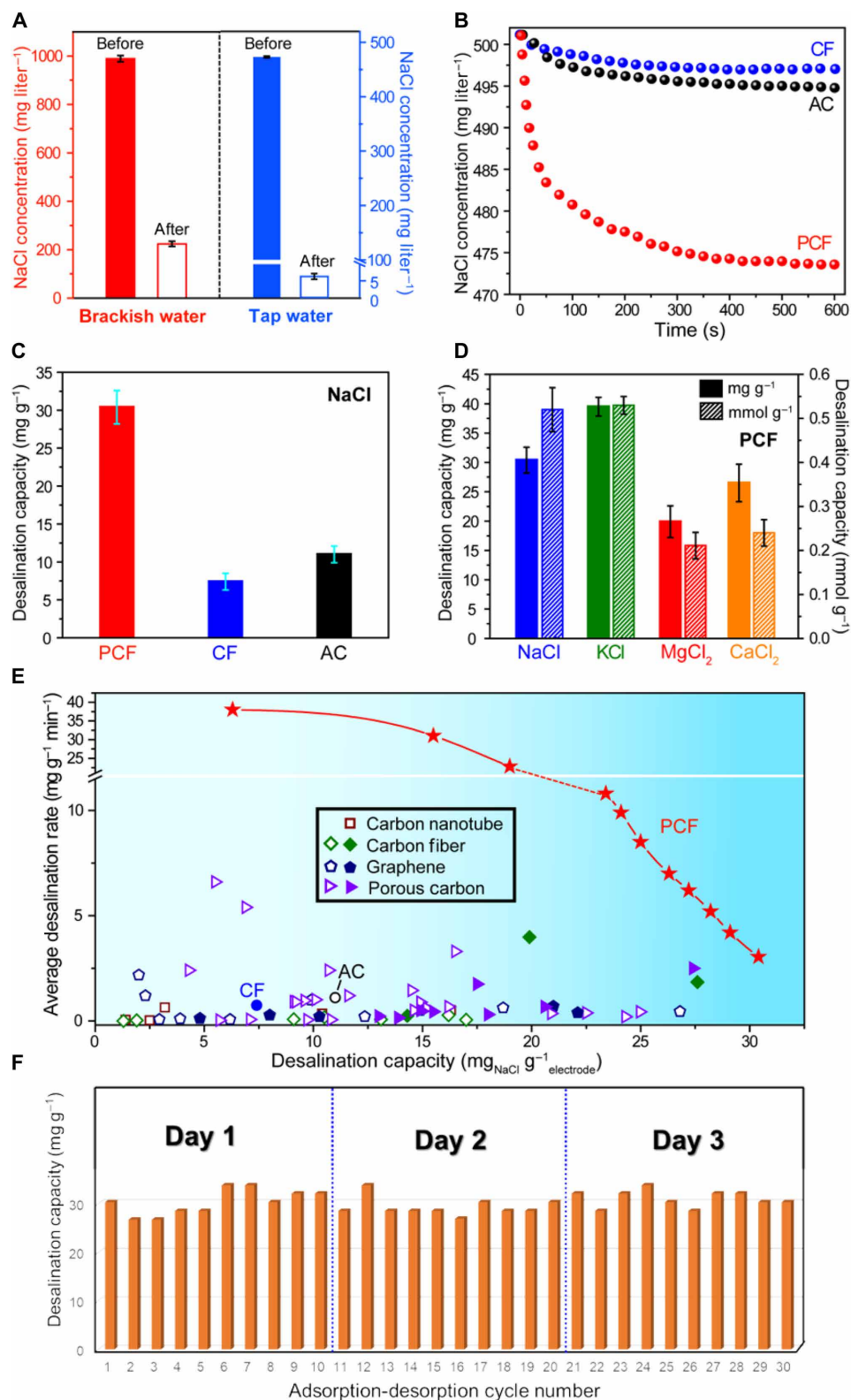
Fig. 5. Desalination performances of PCF, CF, and AC. (**A**) NaCl concentrations in brackish water and tap water before and after deionization by PCF. The NaCl concentrations were determined by ion chromatography. (**B**) Time-resolved NaCl desalination profiles of PCF, CF, and AC in CDI cells with an excess amount of NaCl solution. (**C**) NaCl desalination mass capacities of PCF, CF, and AC. (**D**) Gravimetric and molar desalination capacities of PCF for NaCl, KCl, MgCl₂, and CaCl₂ deionization. (**E**) CDI Ragone plots of PCF, CF, and AC, in comparison with state-of-the-art carbon electrodes. Solid and open symbols are performances of carbon electrodes with and without N-dopants, respectively. The values are summarized in table S2. The lines are a guide to the eye. (**F**) NaCl deionization capacity stability of PCF. The error bars represent 1 SD.

salt concentration is a trade-off between the ion availability for electro-sorption and the co-ion electrostatic repelling within confined pores (39). Upon applying a bias voltage of 1.0 V across the two PCF electrodes (note: a higher bias voltage of 1.2 V triggered oxidation of the tin tape, fig. S6A), the NaCl concentration in the solution decreased from 501.2 to 477.5 mg liter^{-1} within the first 200 s and gradually reached a steady state at 472.8 mg liter^{-1} in the following 400 s (Fig. 5B). The rapidly decreasing NaCl concentration agreed with the current density profiles (fig. S6B). In contrast, in CDI cells containing CF and AC, the NaCl concentrations only experienced slight decreases upon applying the same bias of 1.0 V. After 600 s, CF and AC reduced the salt concentrations from 501.2 to 497.1 mg liter^{-1} and from 501.3 to 495.3 mg liter^{-1}, respectively. On the basis of the salt concentrations before and after desalination, PCF achieved the highest desalination capacity of 30.4 ± 2.2 mg g^{-1}, which was more than four times the capacity of CF (7.4 ± 1.1 mg g^{-1}) and approximately three times that of AC (11.0 ± 1.1 mg g^{-1}) (Fig. 5C). The bare Sn-coated Cu substrates contributed to negligible desalination capacity compared to PCF (fig. S6, C and D). Because of the continuous fibrous carbon to assist rapid electron transfer and the mesopores to allow for fast ion transport, PCF reached an asymptotic desalination capacity within 10 min, corresponding to a time-average desalination rate of ~3.0 mg g^{-1} min^{-1}. To provide a holistic view of the performance, we extracted the desalination capacities and time-average desalination rates at various lengths of time (Fig. 5E). The desalination time of minutes was substantially shorter than those of other porous carbons, which were typically hours. The desalination capacity of PCF outperformed other carbon CDI electrodes (Fig. 5E). The maximal desalination rate of PCF reached 38.0 mg g^{-1} min^{-1}, which was 40 times faster than most carbon electrodes including graphene, carbon nanotubes, CFs, and three-dimensional porous carbons (Fig. 5E and table S2). The high desalination capacity and rate of PCF contributed to an energy-normalized adsorbed salt of 0.75 mg$_{NaCl}$ J^{-1}, equivalent to an energy consumption of 77 kJ mol$_{NaCl}$$^{-1}$. This energy consumption is less than half of the typical reported values (40) and approaches the lower limit of constant-voltage CDI devices under similar testing conditions (41).

PCF was versatile and removed other common cations in water, such as K$^+$, Mg^{2+}, and Ca^{2+} (Fig. 5D). The desalination capacities of PCF for these ions were calculated on the basis of the concentration differences of the corresponding metal chloride solutions before and after applying a bias of 1.0 V for 600 s (fig. S7). The gravimetric desalination capacity of PCF for K$^+$ was the highest (39.5 ± 1.6 mg g^{-1}), followed by Na$^+$ (30.4 ± 2.2 mg g^{-1}), Ca^{2+} (26.5 ± 3.2 mg g^{-1}), and Mg^{2+} (20.9 ± 2.7 mg g^{-1}). To account for the molar masses of different ions, we converted the gravimetric desalination capacities to molar desalination capacities. The molar desalination capacity of PCF decreased in the sequence of K$^+$ (0.53 ± 0.02 mmol g^{-1}), Na$^+$ (0.52 ± 0.05 mmol g^{-1}), Ca^{2+} (0.24 ± 0.03 mmol g^{-1}), and Mg^{2+} (0.21 ± 0.03 mmol g^{-1}). These molar capacities were inversely correlated to the hydrated ion radii, which increases in the sequence of K$^+$ (0.315 nm), Na$^+$ (0.360 nm), Ca^{2+} (0.348 nm), and Mg^{2+} (0.395 nm) (42). This trend, particularly that the molar desalination capacities of divalent ions were about half of those of monovalent ions, suggested that the active materials in this work desalinated water mainly by electrosorption via electrical double layers. Because electrical double-layer CDI involved no chemical reactions to alter the surface of PCF, the desalination capacity showed no substantial loss of desalination capacity after repeated charge-discharge cycles (Fig. 5F). PCF was

subjected to 30 adsorption-desorption cycles with repeated CDI operation, rinsing, drying, and re-hydration for 3 days. After each day, the average desalination capacities of PCF remained at ~30 mg g^{-1}, showing no signs of performance degradation or electrode fouling.

DISCUSSION

Our work highlights that block copolymer–based PCF is a high-performance electrode material for CDI. PCF exhibits an ultrahigh desalination capacity of 30.4 ± 2.2 mg$_{NaCl}$ g$_{PCF}$$^{-1}$, surpassing conventional CF, AC, and other state-of-the-art carbon materials (e.g., carbon nanotubes and graphene) (Fig. 5E and table S2). In addition, PCF displays an ultrafast desalination rate of 38.0 mg g^{-1} min^{-1}, which is approximately 40 times faster than most carbon materials. Besides Na$^+$, PCF can adsorb K$^+$, Mg^{2+}, and Ca^{2+} ions commonly present in saltwater (Fig. 5D). The dependence of desalination capacity on the hydrated ion radius confirms that PCF removes ions mainly via electrical double layers.

The excellent desalination capacity and rate stem from the combined structural, physical, and electrical properties of PCF (Table 1). First, the abundant interconnected and uniform mesopores offer a large ion-accessible surface area. The ion size–based effective desalination surface area constitutes 95.9% of the CO$_2$-based BET surface area, suggesting high ion accessibility to the micropores (Fig. 3C). The interconnected meso- and micropores are responsible for the high ion-accessible surface area and thus the high desalination capacity of PCF, as compared to benchmark materials including CF and AC, which are dominated with micropores. Only 55 and 47% of the CO$_2$-based BET surface areas of CF and AC, respectively, are effective for desalination. Second, the continuous fibrous structure and ion diffusion pathways ensure rapid electron and ion transport across the electrodes (Fig. 1). The four-probe electrical conductivity (Fig. 4D), ion diffusion coefficient (Fig. 4E), cyclic voltammograms (fig. S3E), and electrochemical impedance (fig. S3E) collectively prove that continuous fibrous carbons are more electrically and ionically conductive than AC composed of discrete particles. The electrically conductive fibrous network offers PCF and CF coulombic efficiencies of 72 and 85%, respectively. In contrast, the discrete nature of AC markedly reduces its coulombic efficiency to 47% due to the high internal resistance and high charge dissipation (fig. S6B). The small electrical and ionic resistances of PCF are essential for the high desalination rates. Third, the oxygen and nitrogen heteroatoms (Fig. 4, A and B), which are inherited from PAN and oxidation process, respectively, benefit PCF for CDI: On the one hand, the O and N heteroatoms improve the wettability of PCF to salt solutions (Fig. 4C), which is crucial for high desalination rates. On the other hand, the electronegative N induces local charge redistribution that strengthens ion electrosorption and enhances desalination capacity.

This work shows that PCF is a high-capacity and high-rate material for CDI. Our future work will investigate how the properties of PCF, including PSD, surface area, and heteroatom concentration, influence the desalination performance. We expect a positive correlation between the surface area and desalination capacity of PCF (fig. S8). Thanks to the molecular design, the properties of PCF electrodes for CDI are tunable by the block copolymer composition (43) and pyrolysis conditions (44). Engineering strategies, including coupling PCF with ion-exchange membranes (45, 46), increasing the surface area via physical and chemical activation (e.g., KOH activation) (47), incorporating pseudocapacitive materials (7), and

Table 1. Summary of the structural, elemental, physical, and CDI properties of PCF, CF, and AC.

		PCF	CF	AC
Source		PMMA-*b*-PAN	PAN	Commercial
Physical properties	Peak pore size (nm)	12.7	1.2	2.2
	CO_2 BET surface area ($m^2 g^{-1}$)	132.9 ± 2.4	57.9 ± 1.1	93.8 ± 2.3
	N_2 BET surface area ($m^2 g^{-1}$)	639.9 ± 2.7	144.6 ± 0.2	1317.0 ± 6.0
	Effective desalination surface area ($m^2 g^{-1}$)	127.4	31.8	44.1
	Micropore volume ($cm^3 g^{-1}$)	0.09	0.04	0.06
	Meso- and macro-pore volume ($cm^3 g^{-1}$)	0.32	0.03	0.30
	Contact angle	(Completely wet)	(Completely wet)	95°
Elemental Composition	C (atom %)	81.6	83.1	91.6
	O (atom %)	5.2	6.7	8.2
	Graphitic-N (atom %)	4.9	4.5	0
	Pyridinic-N (atom %)	3.9	3.1	0
	Pyrrolic-N (atom %)	4.4	2.6	0
Electrical properties	Four-probe electrical conductivity (S cm^{-1})	0.97 ± 0.06	1.02 ± 0.06	0.057 ± 0.004
	Equivalent series resistance (ohms)	34.9	34.6	284.1
	Na^+ diffusion coefficient ($\times 10^{-11}$ $cm^2 s^{-1}$)	10.7	0.43	6.2
CDI performance	Desalination capacity ($mg_{NaCl} g_{electrode}^{-1}$)	30	7.4	11
	Desalination rate ($mg_{NaCl} g_{electrode}^{-1} min^{-1}$)	3.0–38	0.74	1.1
	Coulombic efficiency	72%	85%	47%

designing PCF in flow-through continuous desalination cells (*48*) will further boost the desalination capacity and rate.

MATERIALS AND METHODS

Preparation of active materials

PCFs were synthesized from PMMA-*b*-PAN [48-*b*-52 kDa, poly-dispersity index (PDI) = 1.08] following a previous report (*25*). Using reversible addition-fragmentation chain transfer polymerization, methyl methacrylate was first polymerized into PMMA, which was used as a macro chain transfer agent to polymerize the PAN block. PMMA-*b*-PAN was dissolved in DMF at 65°C to form a solution of 16 weight %. The solution was electrospun into PMMA-*b*-PAN fibers under a voltage of 18 kV using a high-voltage power supplier (Model P030HP1, Acopian Technical Company). The as-spun polymer fibers were heated in a tube furnace (Model STF55433C-1, Lindberg/Blue M) in air at 280°C for 8 hours to cross-link and stabilize PAN. Subsequently, the polymer fibers were converted into PCF by annealing at 800°C for 1 hour under a nitrogen atmosphere to carbonize PAN and decompose PMMA. The N_2 flow rate across the tube was 200 standard cubic centimeters per minute. By replacing PMMA-*b*-PAN with PAN (60 kDa, PDI = 1.06), conventional CFs

were prepared according to the same protocol. AC powders were purchased from Stream Chemicals Inc. and used as received.

Preparation of CDI electrodes

PCF, CF, and AC were pressed onto the adhesive side of tin-plated copper tapes (TapeCase, 3M 1183, 3.8 cm by 2.5 cm) using a hydraulic press (Model 46269, Strongway) with a force of 2 metric tons. Mass loadings of the active materials were determined by sub-tracting the mass of the bare tape from the total mass of the working electrode. Typical mass loadings were 7 to 8 mg on each electrode. All masses were measured by an analytical balance with a sensitivity of 0.01 mg.

Materials characterizations

The morphologies of PCF, CF, and AC were imaged by a scanning electron microscope (LEO Zeiss 1550 SEM, 2-kV acceleration voltage, ~2-mm working distance). N_2 and CO_2 physisorption tests were conducted on a 3Flex Pore Analyzer (Micromeritics Instrument Co.) at 77 and 273 K, respectively. Before gas physisorption, all samples were degassed at 90°C for 1 hour and 300°C for 10 hours to remove surface-adsorbed moisture and hydrocarbons. The PSDs were out-lined by NLDFT, following a previous report (*21*). Contact angles

of the electrodes were measured by a goniometer (SL150L KINO) using an aqueous solution of NaCl (500 mg liter^{-1}) as the liquid of interest. Each measurement disposed ~20 μl of liquid. XPS was performed on an XPS microscope (PHI VersaProbe III scanning). All XPS spectra were acquired with a monochromatic Al K_α x-ray (beam energy = 1486.6 eV, beam size = 100 μm in diameter) and dual beam-charge neutralization over a 1400 μm by 100 μm area. All binding energies were calibrated according to the adventitious C 1s peak at 284.8 eV. XPS peak deconvolution was performed using XPSPEAK software. EIS and CVs were acquired using an electrochemical workstation (PARSTATS 4000+, Princeton Applied Research, Ametek Inc.). EIS was performed at open-circuit potentials from 1 to 10,000 Hz with a 5-mV perturbation, using CR2032 coin cells encasing two electrodes with an identical geometric area of 1 cm^2 and NaCl aqueous electrolytes (500 mg liter^{-1}). The electrical resistivities of PCF, CF, and AC were measured by a four-point probe (JANDEL RM3-AR).

Capacitive deionization

The CDI cell is a conical tube containing 20 ml of aqueous salt solutions. The molar total ion concentrations of NaCl, KCl, MgCl$_2$, and CaCl$_2$ were 8.5 mM. Two symmetric electrodes were immersed in the solutions. A four-probe conductivity meter (Model HI-763100 Edge^{EC}, Hanna Instruments) was placed between the two electrodes to monitor the electrical conductivity of the solution. The conductivity meter was calibrated by using two standard solutions of 84 and 5000 μS cm^{-1} (Hanna Instruments) before use. The solution temperature was measured by a temperature sensor built in the electrical conductivity meter. The temperature variation was less than 0.2°C throughout the tests. Alternatively, NaCl concentrations were determined by ion chromatography (Dionex LC20) coupled with an ED40 electrochemical detector. Each injection consumed ~0.5 ml of solution. To avoid detector saturation, solutions before and after deionization were all diluted with deionized water by 5 and 10 times for solutions initially containing NaCl (500 and 1000 mg liter^{-1}, respectively). The desalination potential was set at 1 V to avoid corroding the tin tapes. Before desalination, the two electrodes were soaked in the salt solution without an external bias to stabilize the solution conductivity and minimize the influence of initial physisorption. All salt solutions were prepared with reagent-grade anhydrous salts (NaCl, KCl, MgCl$_2$, and CaCl$_2$; >95%) and deionized water (electrical resistivity ~15 megohms·cm). Electrical conductivities were converted to solution concentrations according to the calibration curves (fig. S5).

SUPPLEMENTARY MATERIALS

Supplementary material for this article is available at http://advances.sciencemag.org/cgi/content/full/6/16/eaaz0906/DC1

REFERENCES AND NOTES

1. M. Rodell, J. S. Famiglietti, D. N. Wiese, J. T. Reager, H. K. Beaudoing, F. W. Landerer, M. H. Lo, Emerging trends in global freshwater availability. *Nature* **557**, 651–659 (2018).
2. H. Y. Yang, Z. J. Han, S. F. Yu, K. L. Pey, K. Ostrikov, R. Karnik, Carbon nanotube membranes with ultrahigh specific adsorption capacity for water desalination and purification. *Nat. Commun.* **4**, 2220 (2013).
3. Z. S. Cao, S. Zeng, Z. Xu, A. Arvanitis, S. Yang, X. Gu, J. Dong, Ultrathin ZSM-5 zeolite nanosheet laminated membrane for high-flux desalination of concentrated brines. *Sci. Adv.* **4**, eaau8634 (2018).
4. S. Porada, R. Zhao, A. van der Wal, V. Presser, P. M. Biesheuvel, Review on the science and technology of water desalination by capacitive deionization. *Prog. Mater. Sci.* **58**, 1388–1442 (2013).
5. L. Wang, J. E. Dykstra, S. Lin, Energy efficiency of capacitive deionization. *Environ. Sci. Technol.* **53**, 3366–3378 (2019).
6. B. W. Byles, D. A. Cullen, K. L. More, E. Pomerantseva, Tunnel structured manganese oxide nanowires as redox active electrodes for hybrid capacitive deionization. *Nano Energy* **44**, 476–488 (2018).
7. Z. Y. Leong, G. Lu, H. Y. Yang, Three-dimensional graphene oxide and polyvinyl alcohol composites as structured activated carbons for capacitive desalination. *Desalination* **451**, 172–181 (2019).
8. Z.-H. Huang, Z. Yang, F. Kang, M. Inagaki, Carbon electrodes for capacitive deionization. *J. Mater. Chem. A* **5**, 470–496 (2017).
9. S. Porada, L. Weinstein, R. Dash, A. van der Wal, M. Bryjak, Y. Gogotsi, P. M. Biesheuvel, Water desalination using capacitive deionization with microporous carbon electrodes. *ACS Appl. Mater. Interfaces* **4**, 1194–1199 (2012).
10. C.-H. Hou, C.-Y. Huang, A comparative study of electrosorption selectivity of ions by activated carbon electrodes in capacitive deionization. *Desalination* **314**, 124–129 (2013).
11. H. Li, T. Lu, L. Pan, Y. Zhang, Z. Sun, Electrosorption behavior of graphene in NaCl solutions. *J. Mater. Chem.* **19**, 6773–6779 (2009).
12. H. Wang, D. Zhang, T. Yan, X. Wen, J. Zhang, L. Shi, Q. Zhong, Three-dimensional macroporous graphene architectures as high performance electrodes for capacitive deionization. *J. Mater. Chem. A* **1**, 11778–11789 (2013).
13. W. Kong, X. Duan, Y. Ge, H. Liu, J. Hu, X. Duan, Holey graphene hydrogel with in-plane pores for high-performance capacitive desalination. *Nano Res.* **9**, 2458–2466 (2016).
14. C. Zhao, G. Liu, N. Sun, X. Zhang, G. Wang, Y. Zhang, H. Zhang, H. Zhao, Biomass-derived N-doped porous carbon as electrode materials for Zn-air battery powered capacitive deionization. *Chem. Eng. J.* **334**, 1270–1280 (2018).
15. C. Feng, Y.-A. Chen, C.-P. Yu, C.-H. Hou, Highly porous activated carbon with multi-channeled structure derived from loofa sponge as a capacitive electrode material for the deionization of brackish water. *Chemosphere* **208**, 285–293 (2018).
16. A. Omosebi, X. Gao, J. Rentschler, J. Landon, K. Liu, Continuous operation of membrane capacitive deionization cells assembled with dissimilar potential of zero charge electrode pairs. *J. Colloid Interface Sci.* **446**, 345–351 (2015).
17. A. C. Forse, J. M. Griffin, C. Merlet, J. Carretero-Gonzalez, A.-R. O. Raji, N. M. Trease, C. P. Grey, Direct observation of ion dynamics in supercapacitor electrodes using in situ diffusion NMR spectroscopy. *Nat. Energy* **2**, 16216 (2017).
18. F. Zhang, T. Liu, M. Li, M. Yu, Y. Luo, Y. Tong, Y. Li, Multiscale pore network boosts capacitance of carbon electrodes for ultrafast charging. *Nano Lett.* **17**, 3097–3104 (2017).
19. C. Péan, C. Merlet, B. Rotenberg, P. A. Madden, P.-L. Taberna, B. Daffos, M. Salanne, P. Simon, On the dynamics of charging in nanoporous carbon-based supercapacitors. *ACS Nano* **8**, 1576–1583 (2014).
20. X. Xu, H. Tan, Z. Wang, C. Wang, L. Pan, Y. V. Kaneti, T. Yang, Y. Yamauchi, Extraordinary capacitive deionization performance of highly-ordered mesoporous carbon nano-polyhedra for brackish water desalination. *Environ. Sci. Nano* **6**, 981–989 (2019).
21. Z. Zhou, T. Liu, A. U. Khan, G. Liu, Block copolymer–based porous carbon fibers. *Sci. Adv.* **5**, eaau6852 (2019).
22. X. Wen, D. Zhang, L. Shi, T. Yan, H. Wang, J. Zhang, Three-dimensional hierarchical porous carbon with a bimodal pore arrangement for capacitive deionization. *J. Mater. Chem.* **22**, 23835–23844 (2012).
23. M. Liu, M. Xu, Y. Xue, W. Ni, S. Huo, L. Wu, Z. Yang, Y.-M. Yan, Efficient capacitive deionization using natural basswood-derived, freestanding, hierarchically porous carbon electrodes. *ACS Appl. Mater. Interfaces* **10**, 31260–31270 (2018).
24. X. Xu, Z. Sun, D. H. C. Chua, L. Pan, Novel nitrogen doped graphene sponge with ultrahigh capacitive deionization performance. *Sci. Rep.* **5**, 11225 (2015).
25. Z. Zhou, G. Liu, Controlling the pore size of mesoporous carbon thin films through thermal and solvent annealing. *Small* **13**, 1603107 (2017).
26. T. Liu, Z. Zhou, Y. Guo, D. Guo, G. Liu, Block copolymer derived uniform mesopores enable ultrafast electron and ion transport at high mass loadings. *Nat. Commun.* **10**, 675 (2019).
27. K. S. W. Sing, D. H. Everett, R. A. W. Haul, L. Moscou, R. A. Pierotti, J. Rouquérol, T. Siemieniewska, Reporting physisorption data for gas/solid systems with special reference to the determination of surface area and porosity. *Pure Appl. Chem.* **57**, 603 (1985).
28. S. M. Khan, Y. Hitayama, Y. Yamada, S. Gohda, H. Ono, D. Umeda, K. Abe, K. Hata, T. Ohba, High CO_2 sensitivity and reversibility on nitrogen-containing polymer by remarkable CO_2 adsorption on nitrogen sites. *J. Phys. Chem. C* **122**, 24143–24149 (2018).
29. F. Stoeckli, T. A. Centeno, On the determination of surface areas in activated carbons. *Carbon* **43**, 1184–1190 (2005).
30. M. Thommes, K. Kaneko, A. V. Neimark, J. P. Olivier, F. Rodriguez-Reinoso, J. Rouquerol, K. S. W. Sing, Physisorption of gases, with special reference to the evaluation of surface area and pore size distribution (IUPAC Technical Report). *Pure Appl. Chem.* **87**, 1051–1069 (2015).
31. S. Porada, L. Borchardt, M. Oschatz, M. Bryjak, J. S. Atchison, K. J. Keesman, S. Kaskel, P. M. Biesheuvel, V. Presser, Direct prediction of the desalination performance of porous carbon electrodes for capacitive deionization. *Energ. Environ. Sci.* **6**, 3700–3712 (2013).

32. T. Liu, F. Zhang, Y. Song, Y. Li, Revitalizing carbon supercapacitor electrodes with hierarchical porous structures. *J. Mater. Chem. A* **5**, 17705–17733 (2017).

33. L. Li, L. Zou, H. Song, G. Morri, Ordered mesoporous carbons synthesized by a modified sol–gel process for electrosorptive removal of sodium chloride. *Carbon* **47**, 775–781 (2009).

34. M. S. A. Rahaman, A. F. Ismail, A. Mustafa, A review of heat treatment on polyacrylonitrile fiber. *Polym. Degrad. Stab.* **92**, 1421–1432 (2007).

35. J.-S. Wei, C. Ding, P. Zhang, H. Ding, X.-Q. Niu, Y.-Y. Ma, C. Li, Y.-G. Wang, H.-M. Xiong, Robust negative electrode materials derived from carbon dots and porous hydrogels for high-performance hybrid supercapacitors. *Adv. Mater.* **31**, 1806197 (2019).

36. X. Xu, A. E. Allah, C. Wang, H. Tan, A. A. Farghali, M. H. Khedr, V. Malgras, T. Yang, Y. Yamauchi, Capacitive deionization using nitrogen-doped mesostructured carbons for highly efficient brackish water desalination. *Chem. Eng. J.* **362**, 887–896 (2019).

37. P. Rani, V. K. Jindal, Designing band gap of graphene by B and N dopant atoms. *RSC Adv.* **3**, 802–812 (2013).

38. H. Su, H. Huang, H. Zhang, X. Chu, B. Zhang, B. Gu, X. Zheng, S. Wu, W. He, C. Yan, J. Chen, W. Yang, In situ direct method to massively prepare hydrophilic porous carbide-derived carbons for high-performance supercapacitors. *ACS Appl. Energy Mater.* **1**, 3544–3553 (2018).

39. P. M. Biesheuvel, S. Porada, M. Levi, M. Z. Bazant, Attractive forces in microporous carbon electrodes for capacitive deionization. *J. Solid State Electrochem.* **18**, 1365–1376 (2014).

40. Y. T. Qu, P. G. Campbell, L. Gu, J. M. Knipe, E. Dzenitis, J. G. Santiago, M. Stadermann, Energy consumption analysis of constant voltage and constant current operations in capacitive deionization. *Desalination* **400**, 18–24 (2016).

41. J. E. Dykstra, S. Porada, A. van der Wal, P. M. Biesheuvel, Energy consumption in capacitive deionization—Constant current versus constant voltage operation. *Water Res.* **143**, 367–375 (2018).

42. Y. Marcus, Ionic radii in aqueous solutions. *Chem. Rev.* **88**, 1475–1498 (1988).

43. J. M. Serrano, T. Liu, A. U. Khan, B. Botset, B. J. Stovall, Z. Xu, D. Guo, K. Cao, X. Hao, S. Cheng, G. Liu, Composition design of block copolymers for porous carbon fibers. *Chem. Mater.* **31**, 8898–8907 (2019).

44. Z. Zhou, T. Liu, A. U. Khan, G. Liu, Controlling the physical and electrochemical properties of block copolymer-based porous carbon fibers by pyrolysis temperature. *Mol. Syst. Des. Eng.* **5**, 153–165 (2020).

45. H. Li, Y. Gao, L. Pan, Y. Zhang, Y. Chen, Z. Sun, Electrosorptive desalination by carbon nanotubes and nanofibres electrodes and ion-exchange membranes. *Water Res.* **42**, 4923–4928 (2008).

46. J. Kamcev, D. R. Paul, B. D. Freeman, Equilibrium ion partitioning between aqueous salt solutions and inhomogeneous ion exchange membranes. *Desalination* **446**, 31–41 (2018).

47. G. Wang, Q. Dong, Z. Ling, C. Pan, C. Yu, J. Qiu, Hierarchical activated carbon nanofiber webs with tuned structure fabricated by electrospinning for capacitive deionization. *J. Mater. Chem.* **22**, 21819–21823 (2012).

48. M. E. Suss, T. F. Baumann, W. L. Bourcier, C. M. Spadaccini, K. A. Rose, J. G. Santiago, M. Stadermann, Capacitive desalination with flow-through electrodes. *Energ. Environ. Sci.* **5**, 9511–9519 (2012).

49. D. Qu, G. Wang, J. Kafle, J. Harris, L. Crain, Z. Jin, D. Zheng, Electrochemical impedance and its applications in energy-storage systems. *Small Methods* **2**, 1700342 (2018).

50. T. Kim, J. E. Dykstra, S. Porada, A. van der Wal, J. Yoon, P. M. Biesheuvel, Enhanced charge efficiency and reduced energy use in capacitive deionization by increasing the discharge voltage. *J. Colloid Interface Sci.* **446**, 317–326 (2015).

51. F. Ehrburger-Dolle, M. Holz, J. Lahaye, Use of N_2, Ar and CO_2 adsorption for the determination of microporosity and surface fractal dimension of carbon blacks and silicas. *Pure Appl. Chem.* **65**, 2223–2230 (1993).

52. K. C. Kim, T.-U. Yoon, Y.-S. Bae, Applicability of using CO_2 adsorption isotherms to determine BET surface areas of microporous materials. *Micropor. Mesopor. Mat.* **224**, 294–301 (2016).

53. H. Li, L. Pan, Y. Zhang, L. Zou, C. Sun, Y. Zhan, Z. Sun, Kinetics and thermodynamics study for electrosorption of NaCl onto carbon nanotubes and carbon nanofibers electrodes. *Chem. Phys. Lett.* **485**, 161–166 (2010).

54. L. Wang, M. Wang, Z.-H. Huang, T. Cui, X. Gui, F. Kang, K. Wang, D. Wu, Capacitive deionization of NaCl solutions using carbon nanotube sponge electrodes. *J. Mater. Chem. A* **21**, 18295–18299 (2011).

55. A. Aldalbahi, M. Rahaman, M. Almoiqli, A. Hamedelniel, A. Alrehaili, Single-walled carbon nanotube (SWCNT) loaded porous reticulated vitreous carbon (RVC) electrodes used in a capacitive deionization (CDI) cell for effective desalination. *Nanomaterials* **8**, 527 (2018).

56. X. Xu, Y. Liu, T. Lu, Z. Sun, D. H. C. Chua, L. Pan, Rational design and fabrication of graphene/carbon nanotubes hybrid sponge for high-performance capacitive deionization. *J. Mater. Chem. A* **3**, 13418–13425 (2015).

57. S. Wang, D. Z. Wang, L. J. Ji, Q. Gong, Y. F. Zhu, J. Liang, Equilibrium and kinetic studies on the removal of NaCl from aqueous solutions by electrosorption on carbon nanotube electrodes. *Sep. Purif. Technol.* **58**, 12–16 (2007).

58. M. Wang, Z.-H. Huang, L. Wang, M.-X. Wang, F. Kang, H. Hou, Electrospun ultrafine carbon fiber webs for electrochemical capacitive desalination. *New J. Chem.* **34**, 1843–1845 (2010).

59. J. Liu, S. Wang, J. Yang, J. Liao, M. Lu, H. Pan, L. An, $ZnCl_2$ activated electrospun carbon nanofiber for capacitive desalination. *Desalination* **344**, 446–453 (2014).

60. A. G. El-Deen, N. A. M. Barakat, K. A. Khalil, H. Y. Kim, Hollow carbon nanofibers as an effective electrode for brackish water desalination using the capacitive deionization process. *New J. Chem.* **38**, 198–205 (2014).

61. Y. Belaustegui, S. Zorita, F. Fernández-Carretero, A. García-Luis, F. Pantò, S. Stelitano, P. Frontera, P. Antonucci, S. Santangelo, Electro-spun graphene-enriched carbon fibres with high nitrogen-contents for electrochemical water desalination. *Desalination* **428**, 40–49 (2018).

62. G. Zhu, H. Wang, H. Xu, L. Zhang, Enhanced capacitive deionization by nitrogen-doped porous carbon nanofiber aerogel derived from bacterial-cellulose. *J. Electroanal. Chem.* **822**, 81–88 (2018).

63. Y. Li, Y. Liu, M. Wang, X. Xu, T. Lu, C. Q. Sun, L. Pan, Phosphorus-doped 3D carbon nanofiber aerogels derived from bacterial-cellulose for highly-efficient capacitive deionization. *Carbon* **130**, 377–383 (2018).

64. N. Pugazhenthiran, S. Sen Gupta, A. Prabhath, M. Manikandan, J. R. Swathy, V. K. Raman, T. Pradeep, Cellulose derived graphenic fibers for capacitive desalination of brackish water. *ACS Appl. Mater. Interfaces* **7**, 20156–20163 (2015).

65. W. Shi, H. Li, X. Cao, Z. Y. Leong, J. Zhang, T. Chen, H. Zhang, H. Y. Yang, Ultrahigh performance of novel capacitive deionization electrodes based on a three-dimensional graphene architecture with nanopores. *Sci. Rep.* **6**, 18966 (2016).

66. X. Wen, D. Zhang, T. Yan, J. Zhang, L. Shi, Three-dimensional graphene-based hierarchically porous carbon composites prepared by a dual-template strategy for capacitive deionization. *J. Mater. Chem. A* **1**, 12334–12344 (2013).

67. X. Xu, L. Pan, Y. Liu, T. Lu, Z. Sun, Enhanced capacitive deionization performance of graphene by nitrogen doping. *J. Colloid Interface Sci.* **445**, 143–150 (2015).

68. H. Wang, L. Shi, T. Yan, J. Zhang, Q. Zhong, D. Zhang, Design of graphene-coated hollow mesoporous carbon spheres as high performance electrodes for capacitive deionization. *J. Mater. Chem. A* **2**, 4739–4750 (2014).

69. O. Noonan, Y. Liu, X. Huang, C. Yu, Layered graphene/mesoporous carbon heterostructures with improved mesopore accessibility for high performance capacitive deionization. *J. Mater. Chem. A* **6**, 14272–14280 (2018).

70. H. Yin, S. Zhao, J. Wan, H. Tang, L. Chang, L. He, H. Zhao, Y. Gao, Z. Tang, Three-dimensional graphene/metal oxide nanoparticle hybrids for high-performance capacitive deionization of saline water. *Adv. Mater.* **25**, 6270–6276 (2013).

71. X. Xu, L. Pan, Y. Liu, T. Lu, Z. Sun, D. H. C. Chua, Facile synthesis of novel graphene sponge for high performance capacitive deionization. *Sci. Rep.* **5**, 8458 (2015).

72. T. Yan, J. Liu, H. Lei, L. Shi, Z. An, H. S. Park, D. Zhang, Capacitive deionization of saline water using sandwich-like nitrogen-doped graphene composites via a self-assembling strategy. *Environ. Sci. Nano* **5**, 2722–2730 (2018).

73. Z. U. Khan, T. Yan, L. Shi, D. Zhang, Improved capacitive deionization by using 3D intercalated graphene sheet–sphere nanocomposite architectures. *Environ. Sci. Nano* **5**, 980–991 (2018).

74. P. Zhang, P. A. Fritz, K. Schroën, H. Duan, R. M. Boom, M. B. Chan-Park, Zwitterionic polymer modified porous carbon for high-performance and antifouling capacitive desalination. *ACS Appl. Mater. Interfaces* **10**, 33564–33573 (2018).

75. C. Tsouris, R. Mayes, J. Kiggans, K. Sharma, S. Yiacoumi, S. DePaoli, S. Dai, Mesoporous carbon for capacitive deionization of saline water. *Environ. Sci. Technol.* **45**, 10243–10249 (2011).

76. P. Xu, J. E. Drewes, D. Heil, G. Wang, Treatment of brackish produced water using carbon aerogel-based capacitive deionization technology. *Water Res.* **42**, 2605–2617 (2008).

77. Z. Chen, H. Zhang, C. Wu, L. Luo, C. Wang, S. Huang, H. Xu, A study of the effect of carbon characteristics on capacitive deionization (CDI) performance. *Desalination* **433**, 68–74 (2018).

78. S. Zhao, T. Yan, H. Wang, G. Chen, L. Huang, J. Zhang, L. Shi, D. Zhang, High capacity and high rate capability of nitrogen-doped porous hollow carbon spheres for capacitive deionization. *Appl. Surf. Sci.* **369**, 460–469 (2016).

79. Y. Liu, T. Chen, T. Lu, Z. Sun, D. H. C. Chua, L. Pan, Nitrogen-doped porous carbon spheres for highly efficient capacitive deionization. *Electrochim. Acta* **158**, 403–409 (2015).

80. Q. Liu, X. Li, Y. Wu, M. Qing, G. Tan, D. Xiao, Pine pollen derived porous carbon with efficient capacitive deionization performance. *Electrochim. Acta* **298**, 360–371 (2019).

81. C.-L. Yeh, H.-C. Hsi, K.-C. Li, C.-H. Hou, Improved performance in capacitive deionization of activated carbon electrodes with a tunable mesopore and micropore ratio. *Desalination* **367**, 60–68 (2015).

82. M. Wang, X. Xu, J. Tang, S. Hou, M. S. A. Hossain, L. Pan, Y. Yamauchi, High performance capacitive deionization electrodes based on ultrathin nitrogen-doped carbon/graphene nano-sandwiches. *Chem. Commun.* **53**, 10784–10787 (2017).

83. F. Ji, L. Wang, J. Yang, X. Wu, M. Li, S. Jiang, S. Lin, Z. Chen, Highly compact, free-standing porous electrodes from polymer-derived nanoporous carbons for efficient electrochemical capacitive deionization. *J. Mater. Chem. A* **7**, 1768–1778 (2019).

84. B. Krüner, P. Srimuk, S. Fleischmann, M. Zeiger, A. Schreiber, M. Aslan, A. Quade, V. Presser, Hydrogen-treated, sub-micrometer carbon beads for fast capacitive deionization with high performance stability. *Carbon* **117**, 46–54 (2017).

85. T. Kim, J. Yoon, CDI ragone plot as a functional tool to evaluate desalination performance in capacitive deionization. *RSC Adv.* **5**, 1456–1461 (2015).

86. D. Sriramulu, S. Vafakhah, H. Y. Yang, Activated *Luffa* derived biowaste carbon for enhanced desalination performance in brackish water. *RSC Adv.* **9**, 14884–14892 (2019).

87. J. Zhang, J. Fang, J. Han, T. Yan, L. Shi, D. Zhang, N, P, S co-doped hollow carbon polyhedra derived from MOF-based core–shell nanocomposites for capacitive deionization. *J. Mater. Chem. A* **6**, 15245–15252 (2018).

Citation: T. Liu, J. Serrano, J. Elliott, X. Yang, W. Cathcart, Z. Wang, Z. He, G. Liu, Exceptional capacitive deionization rate and capacity by block copolymer–based porous carbon fibers. *Sci. Adv.* **6**, eaaz0906 (2020).